Supplementary Information

Regulating the thickness of NiO layer to optimize the photoinduced carrier separation behavior of $BiVO_4$

Yaru Peng [a, b], Junhao Cai [a] and Guoqiang Li [a, c]*

a. International Joint Research Laboratory of New Energy Materials and Devices of Henan Province, School of Physics and Electronics, Henan University, Kaifeng, 475004, PR China

b. College of Electronics and Engineering, North China University of Water Resources and Electric Power, Zhengzhou 450046, PR China

c. National Demonstration Center for Experimental Physics and Electronics Education, School of Physics and Electronics, Henan University, Kaifeng, 475004, PR China

*Corresponding authors. E-mail addresses: gqli1980@henu.edu.cn

The production of H_2O_2 was detected using Cu^{2+} and DMP spectrophotometry. The principle is to reduce Cu^{2+} with H_2O_2 generated during the photocatalytic process, and form a bright yellow and stable $Cu(DMP)_2^+$complex with DMP solution under natural light. Its maximum absorbance is 454 nm, as shown in Fig. S1. The stoichiometry is: $2Cu^{2+} + 4DMP + H_2O_2 \rightarrow 2Cu(DMP)_2^{+} + O_2 + 2H^{+}$. By establishing the corresponding relationship between the absorption value of $Cu(DMP)_2^+$ and the standard concentration of H_2O_2, the production of H_2O_2 in the photocatalytic process of the sample can be determined.

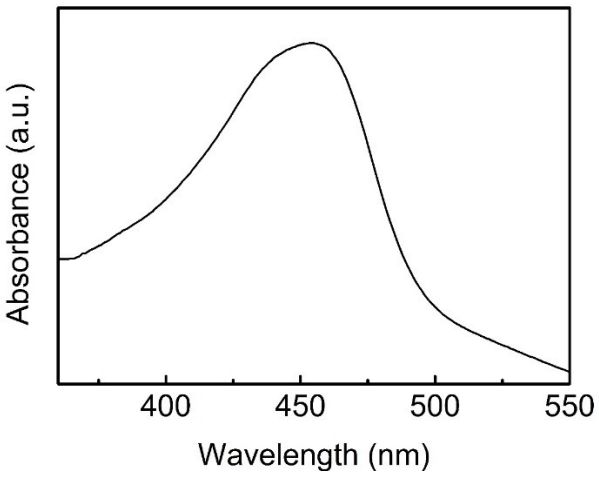

Fig. S1 Absorption spectrum of $Cu(DMP)_2^+$ at a wavelength of 454 nm.

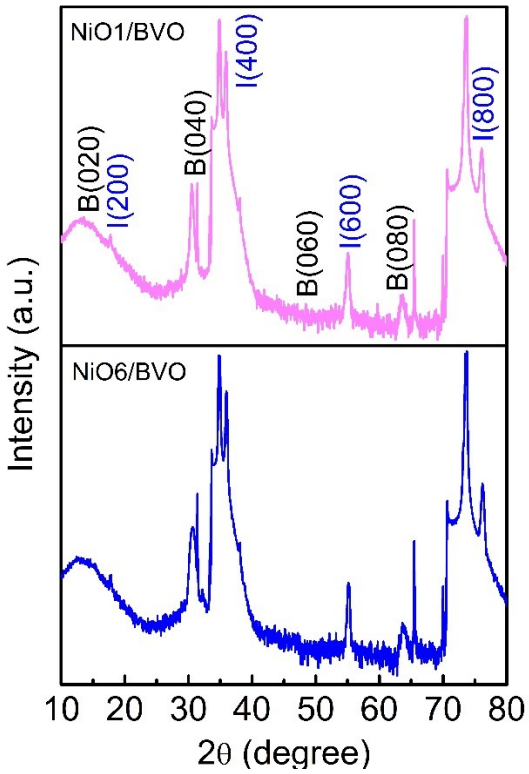

Fig. S2 XRD patterns of NiO1/BVO and NiO6/BVO. Mark (B) for BVO (0k0), (I) for ITO (h00).

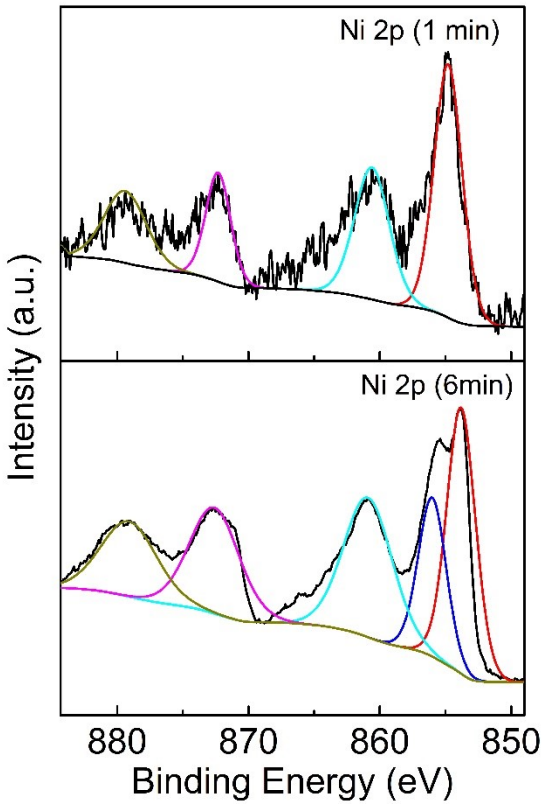

Fig. S3 The binding energy of Ni 2p in NiO1/BVO and NiO6/BVO.

Fig. S4(a) presents the high-resolution XPS spectra of O 1s for BVO and NiO3/BVO. For the BVO sample, the O 1 s XPS profile was deconvoluted into three peaks at 532.22 eV, 530.94 eV, and 529.38 eV, which were assigned to water molecule, adsorbed oxygen, and lattice oxygen, respectively. The O 1 s XPS profile of NiO3/BVO was deconvoluted into three peaks at 531.67, 530.87, and 529.48 eV, which can be attributed to water molecule, adsorbed oxygen, and lattice oxygen, respectively. The area ratio of water molecule, adsorbed oxygen, and lattice oxygen was 0.53:0.11:1 in BVO. Meanwhile, the area ratio of water molecule, adsorbed oxygen, and lattice oxygen was 0.97: 0.02: 1 in NiO3/BVO. The above results indicated that the adsorbed oxygen in heterojunctions was less than that in pure BVO.

Furthermore, the EPR spectra shown in Fig. S4(b) exhibits symmetric peaks

centered around g=2.003 for both samples, indicating the presence of stable oxygen vacancy defects in the samples. The EPR signal intensity in NiO3/BVO is higher than that in BVO, further suggesting the introduction of more oxygen vacancy defects after forming the heterojunction.

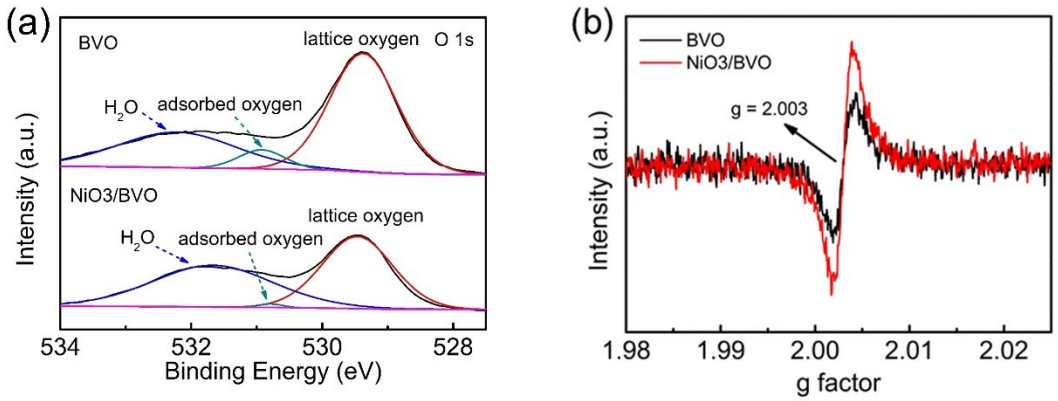

Fig. S4 (a) High-resolution XPS spectra of O 1s and (b) EPR spectrum of BVO and NiO3/BVO samples.

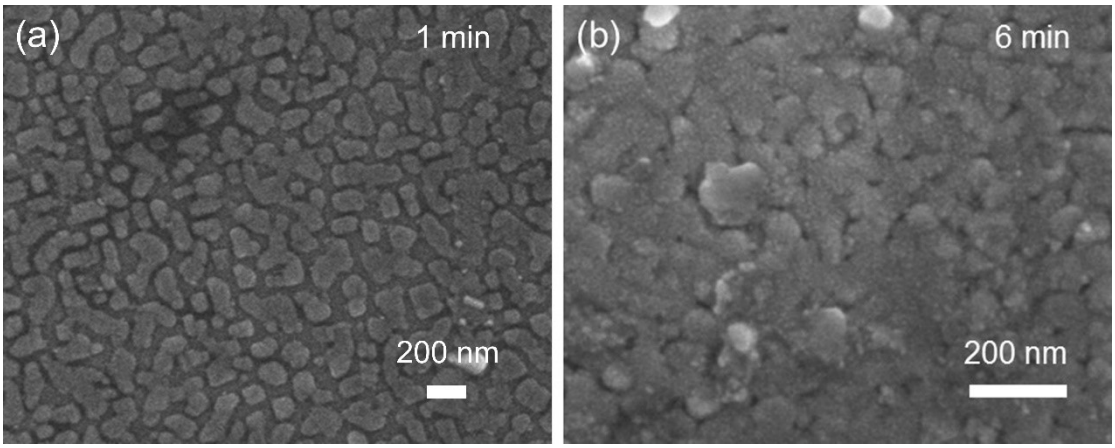

Fig. S5 SEM images of (a) NiO1/BVO and (b) NiO6/BVO.

The effect of deposition time on the film morphology is analyzed using AFM. As shown in Fig. S6(a), due to the limitation of three-dimensional (Volmer-Weber) growth mode, BVO exhibits island growth with sizes ranging from tens to hundreds

of nanometers. Fig. S6(b)-S6(d) show the AFM images of NiO composite films deposited for 1 min, 3 min, and 6 min, respectively. It can be observed that the surface of the films becomes blurred and patterned after NiO layer deposition. At a deposition time of 6 min, the morphology shows a distinct granular structure.

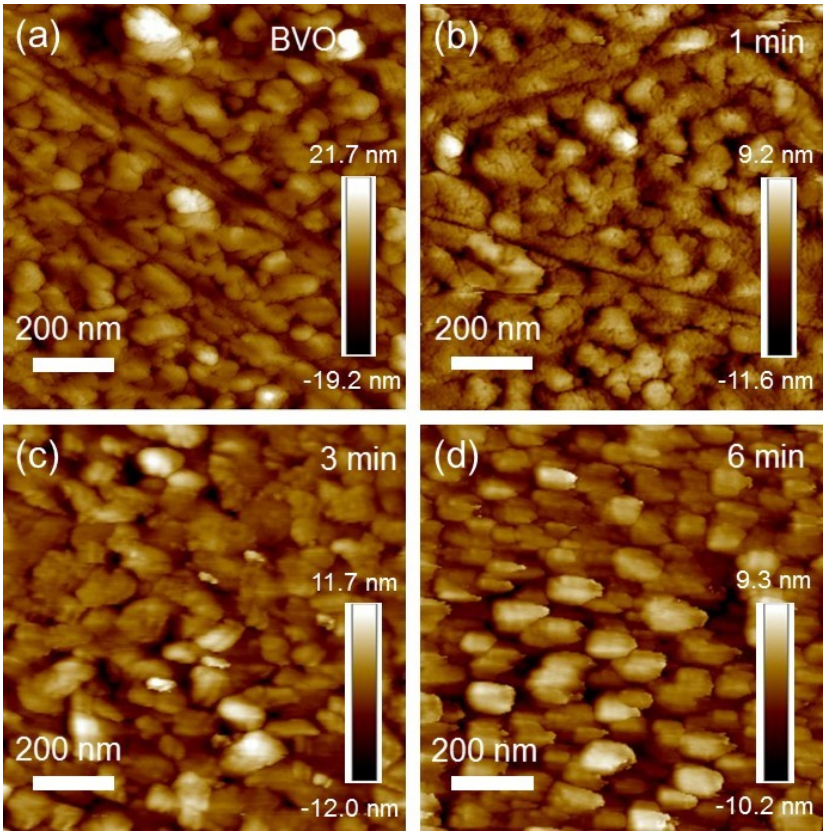

Fig. S6 AFM images of (a) BVO and NiO/BVO with different NiO deposition times (b) 1 min, (c) 3 min, and (d) 6 min.

The roughness of the samples as a function of deposition time is shown in Fig. S7. Compared to BVO, the roughness of the samples significantly decreases after NiO deposition, and there is little change in roughness with increasing deposition time.

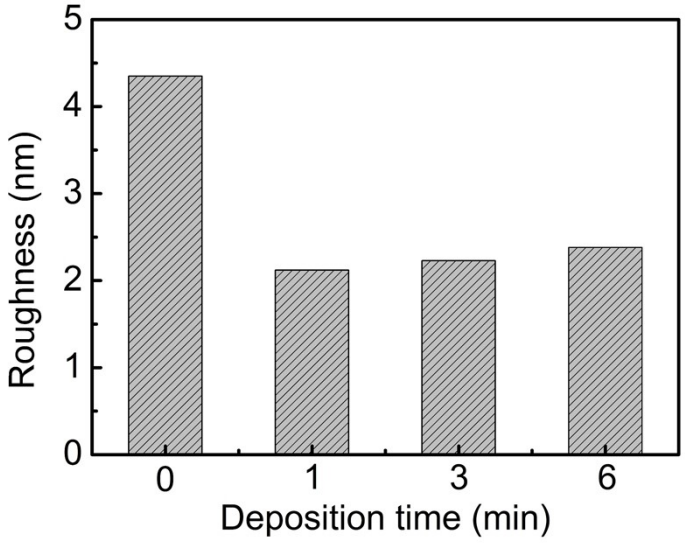

Fig. S7 The variation of sample roughness with NiO deposition time.

To detect the corresponding relationship between the absorption of the product $Cu(DMP)_2^+$ at 454 nm and the concentration of H_2O_2 in the process of photocatalytic reaction, the calibration curve was obtained by adding different standard concentrations of H_2O_2 to the blank solution. As shown in Fig. S8, a linear dependence of absorbance on peroxide concentration in the final measured solution.

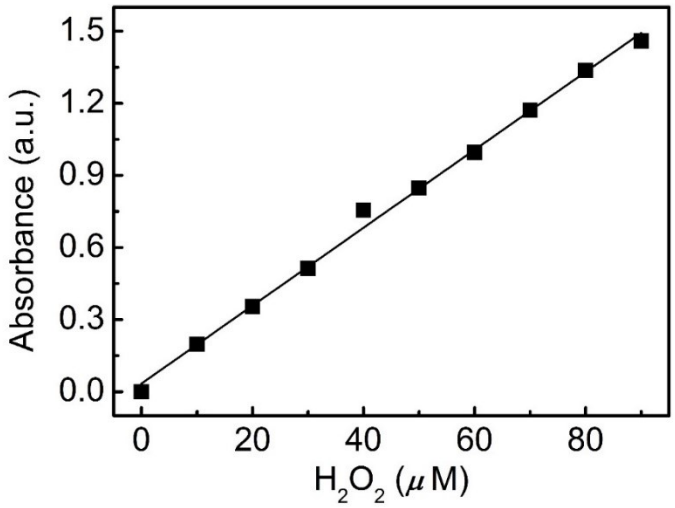

Fig. S8 Calibration curve of H_2O_2 concentration.

A decomposition experiment of H_2O_2 was performed with NiO3/BVO in solution containing H_2O_2 (10 mM) under an Ar atmosphere, where water, EtOH/water (9/1 v/v), and aqueous $NaIO_3$ solution (0.05 M) were used as solvents. EtOH as a sacrificial electron donor, $NaIO_3$ was used in place of usually employed $AgNO_3$ to suppress the deposition of Ag metals on the catalyst.

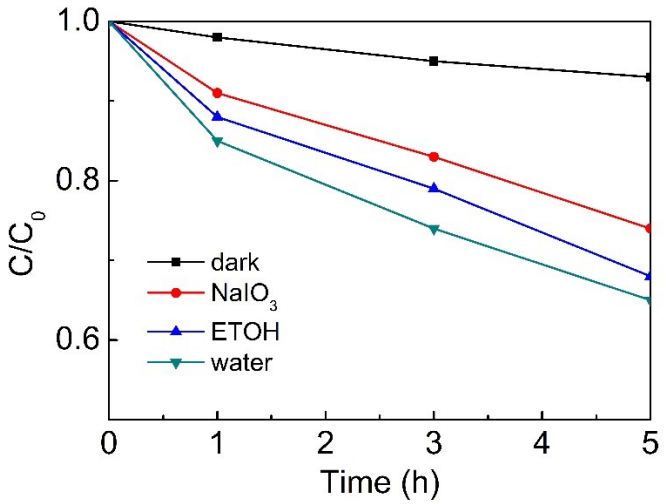

Fig. S9 Results for H_2O_2 decomposition on NiO3/BVO in the dark or under 440 nm monochromatic light.

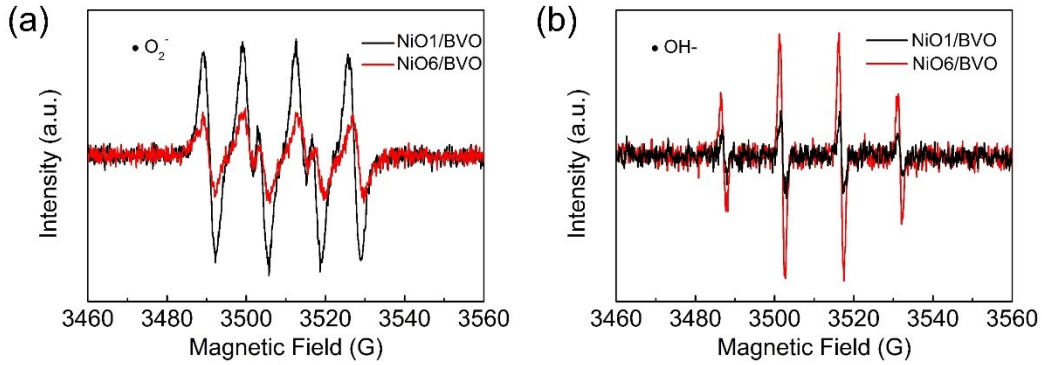

Fig. 10 DMPO spin trapping EPR spectra of NiO1/BVO and NiO6/BVO (a) $\cdot O_2^-$ and (b) ·OH in 440 nm monochromatic light illumination for 5 min.

To further demonstrate the enhanced spatial separation of photoinduced electrons and holes in the NiO/BVO composite film, the PL spectra were utilized to characterize the separation performance of the electron-hole pairs, as shown in Fig. S11. Under excitation at a wavelength of 440 nm, both BVO and NiO3/BVO samples exhibits emission peaks in the range of 480-550 nm (Fig. S11(a)). The BVO displays the strongest luminescent signal, which is attributed to severe charge recombination. In contrast, compared with BVO, the luminescence intensity of NiO3/BVO is significantly reduced, indicating that covering the NiO layer effectively promotes charge spatial separation and prevents electron-hole recombination. In addition, TRPL was applied to research the electron lifetime (Fig. S11(b)), where BVO exhibited an electron lifetime of 2.64 ns, While NiO3/BVO showed a lifetime of 3.58 ns.

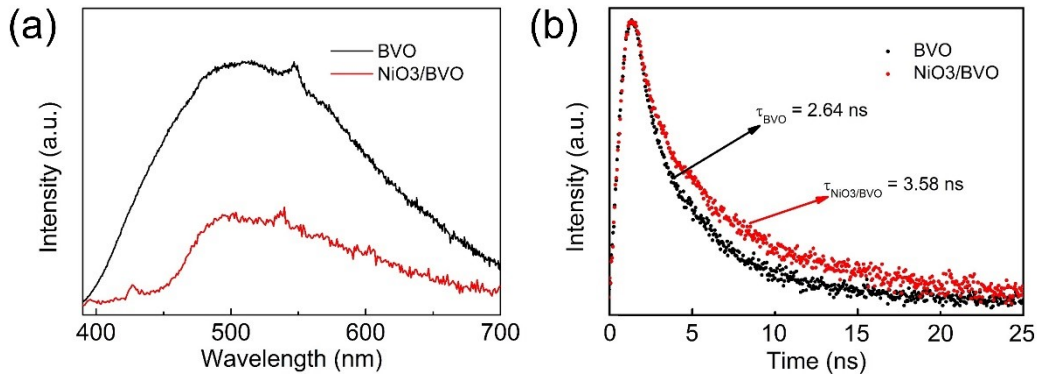

Fig. S11 The PL (a) and TRPL (b) spectra of BVO and NiO3/BVO.

Fig. S12 presents the UV-vis absorption spectra of the BVO and NiO/BVO samples with different NiO deposition times. Pure BVO exhibits visible light absorption in the range of 400-450 nm. Upon deposition of NiO onto BVO, a significant enhancement in the absorption peak intensity is observed, accompanied by a redshift in the absorption edge within a certain range. As the NiO deposition time increases, the absorption peak intensity initially strengthens and then weakens. Specifically, the sample deposited for 3 min shows the highest absorption peak intensity and the greatest redshift in the absorption edge.

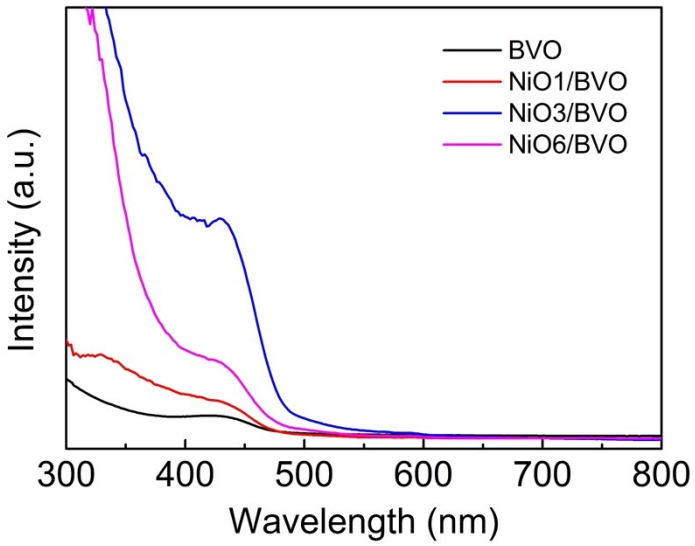

Fig. S12 The UV-vis absorption spectra of BVO and NiO/BVO.

Tauc analysis of the UV-vis absorption spectra revealed that BVO thin film, as a direct bandgap semiconductor material, has an optical bandgap of 2.59 eV, as shown in Fig. S13.

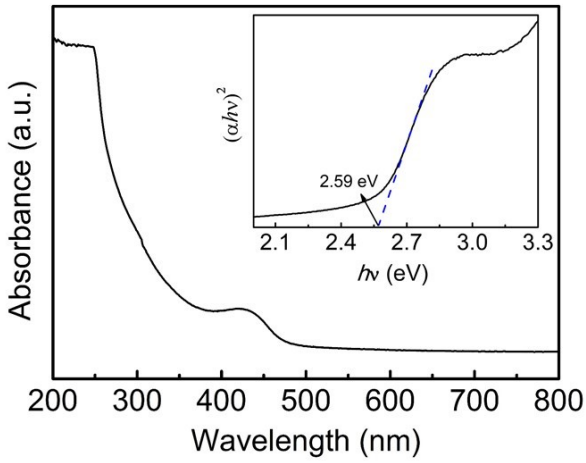

Fig. S13 The UV-vis absorption spectrum of BVO, the upper right inset is optical band gap plot of BVO.

As shown in Fig. S14, in-situ XPS characterization of NiO3/BVO was carried

out under dark and 440 nm monochromatic light irradiation. The binding energies of Ni $2p_{3/2}$ orbitals are 853.22 eV and 853.37 eV, and the binding energies of Ni $2p_{1/2}$ orbitals are 871.12 eV and 871.98 eV under dark and light conditions, respectively. The additional holes in the valence band will lead to more hole states appearing at the Fermi level, which affects the electronic structure and energy level distribution of the material. This effect typically results in an increase in the energy levels of the valence band. The increase in binding energy of Ni 2p observed in the figure under light illumination, proving that in the NiO3/BVO composite structure, holes are transferred from the valence band of BVO to NiO.

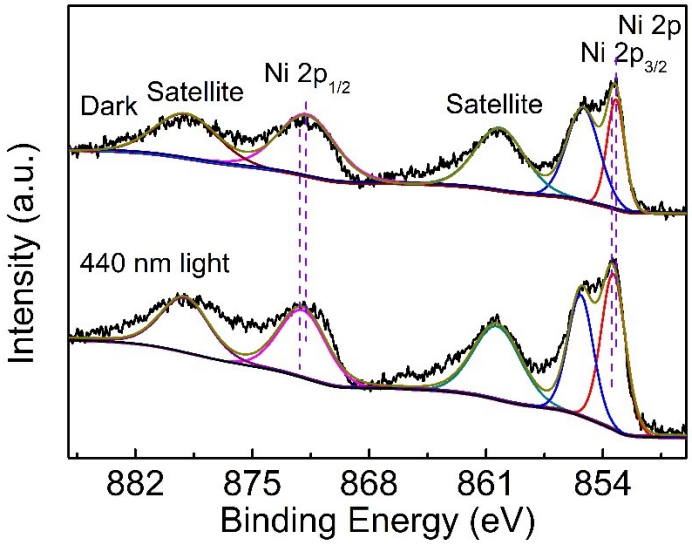

Fig. S14 In-situ Ni 2p XPS spectra of NiO3/BVO.

Table S1 Summary of the photocatalytic properties of the semiconductor materials for

photocatalytic H_2O_2 production

Photocatalyst	Light source	H_2O_2 productivity/h	Notes	References
$Au/BiVO_4$	Visible light	4 μM	50 mg	[1]
Defective BVO	> 420 nm	290 μM	30 mg	[2]
$CoP/Co_2P/BVO$	Sunlight irradiation	9.6 μmol cm^{-2}	Film	[3]
BVO(010)-AuPd	> 420 nm	1.1 mM	80 mg	[4]
Cu@Au/BVO	> 420 nm	30 μM	100 mg	[5]
Au/C_3N_4	Visible light	66 μM	400 mg	[6]
$g\text{-}C_3N_4$	Visible light	27 μM	20 mg	[7]
TiO_2	UV irradiation	96 μM	300 mg	[8]
Pd/TiO_2	Sunlight irradiation	150 μM	5 mg	[9]
$SN\text{-}GQD/TiO_2$	Visible light	451 μM	25 mg	[10]
CdS-RGO	Sunlight irradiation	11 μM	50 mg	[11]
Atomic $Au@MoS_2$	Sunlight irradiation	132 μM	50 mg	[12]
BVO	440 nm monochromatic light	1.74×10^{-2} μM	0.012 mg	This work
NiO/BVO	440 nm monochromatic light	4.59×10^{-2} μM	0.021 mg	

References

1 H. Hirakawa, S. Shiota, Y. Shiraishi, H. Sakamoto, S. Ichikawa and T. Hirai, ACS Catal., 2016, **6**, 4976-4982.

2 M. Sun, X. Wang, H. Pan, Z. Pang and Y. Zhang, J. Colloid Interf. Sci., 2023, **629**, 215-224.

3 Y. Xu, Y. Cao, L. Tan, Q. Chen and Y. Fang, J. Colloid Interf. Sci., 2023, **633**, 323-332.

4 H. Shi, Y. Li, K. Wang, S. Li, X. Wang, P. Wang, F. Chen and H. Yu, Chem. Eng. J., 2022, **443**, 136429.

5 K. Wang, M. Wang, J. Yu, D. Liao, H. Shi, X. Wang and H. Yu, ACS Appl. Nano Mater., 2021, **4**, 13158-13166.

6 G. Zuo, S. Liu, L. Wang, H. Song, P. Zong, W. Hou, B. Li, Z. Guo, X. Meng, Y. Du, T. Wang and V.A.L. Roy, Catal. Commun., 2019, **123**, 69-72.

7 G.-h. Moon, M. Fujitsuka, S. Kim, T. Majima, X. Wang and W. Choi, ACS Catal., 2017, **7**, 2886-2895.

8 R. Cai, Y. Kubota and A. Fujishima, J. Catal. 2003, **219**, 214-218.

9 C. Chu, D. Huang, Q. Zhu, E. Stavitski, J. A. Spies, Z. Pan, J. Mao, H. L. Xin, C. A. Schmuttenmaer, S. Hu and J. H. Kim, ACS Catal., 2018, **9**, 626-631.

10 L. Zheng, H. Su, J. Zhang, L. S. Walekar, H. V. Molamahmood, B. Zhou, M. Long and Y. H. Hu, Appl. Catal. B: Environ., 2018, **239**, 475-484.

11 S. Thakur, T. Kshetri, N. H. Kim and J. H. Lee, J. Catal., 2017, **345**, 78-86.

12 H. Song, L. Wei, C. Chen, C. Wen and F. Han, J. Catal., 2019, **376**, 198-208.